

Preferential concentration by mechanically-driven turbulence in the two-fluid formalism

Sara Nasab* and Pascale Garaud†

Department of Applied Mathematics, Baskin School of Engineering,

University of California Santa Cruz,

1156 High Street, Santa Cruz, CA 95064, USA

arXiv:2103.08121v1 [physics.flu-dyn] 15 Mar 2021

Abstract

Preferential concentration is thought to play a key role in promoting particle growth, which is crucial to processes such as warm rain formation in clouds, planet formation, and industrial sprays. In this work, we investigate preferential concentration using 3D Direct Numerical Simulations adopting the Eulerian-Eulerian two-fluid approach, where the particles are treated as a continuum field with its own momentum and mass conservation laws. We consider particles with Stokes number $St \lesssim O(0.01)$ in moderately turbulent flows with fluid Reynolds number $Re \leq 600$. In our previous work (Nasab & Garaud, *Physical Review Fluids*. doi: 10.1103/PhysRevFluids.5.114308, 2020), we established scaling laws to predict maximum and typical particle concentration enhancements in the context of the particle-driven convective instability. Here we verify that the same results apply when turbulence is externally driven, extending the relevance of our model to a wider class of particle-laden flows. We find in particular that (i) the maximum particle concentration enhancement above the mean scales as $u_{rms}^2 \tau_p / \kappa_p$, where u_{rms} is the rms fluid velocity, τ_p is the particle stopping time, and κ_p is the assumed particle diffusivity from the two-fluid equations; (ii) the typical particle concentration enhancement over the mean scales as $(u_{rms}^2 \tau_p / \kappa_p)^{1/2}$; and (iii) the probability distribution function of the particle concentration enhancement over the mean has an exponential tail whose slope scales like $(u_{rms}^2 \tau_p / \kappa_p)^{-1/2}$. We conclude by discussing the caveats of our model and its implications in a relevant cloud application.

I. INTRODUCTION

Particle-laden flows are a special class of two-phase fluid flows, characterized by a continuous carrier phase and a dispersed, and typically dilute, particle phase. They appear in numerous physical and engineering applications, including for instance clouds, turbidity currents, protoplanetary disks, and industrial sprays. An important physical process in such flows is the tendency of inertial particles to accumulate in regions of high strain and low vorticity [1], otherwise known as preferential concentration. This process is thought to play a fundamental role in promoting collisional growth. In clouds for example, the growth of micron-size to millimeter size droplets is not quite understood. Although processes such

* snasab@ucsc.edu

† pgaraud@ucsc.edu

as Brownian motion and condensation can contribute to droplet growth, it is thought that they alone cannot promote sufficient growth to initiate rainfall. For this reason, preferential concentration is considered to be the key process that may result in the enhanced collision rates required for larger raindrop formation [2–4]. Similarly in accretion disks, preferential concentration is widely hypothesized to be a vital process for the growth of dust particles into planetesimals [5, 6]. Thus, our primary goal is to investigate and quantify particle concentration enhancement due to preferential concentration in turbulent flows.

In this work (as also in Nasab and Garaud [7]), we use the two-fluid formalism and treat the particles as a continuous phase of the system that is distinct from the carrier fluid (see Crowe et al. [8], Elghobashi [9], Morel [10] and references within). This continuum approximation is derived by applying techniques motivated by kinetic theory in which the positions and velocities of the particles are statistically averaged to create a local particle density ρ_p and velocity \mathbf{u}_p . We focus on the case where the solid density of the particle ρ_s is much greater than the mean density of the carrier flow ρ_f , which is true for many applications. In this limit, the importance of particle inertia is traditionally measured by the Stokes number $St = \tau_p/\tau_e$, defined as the ratio of the particle stopping time τ_p to the eddy turnover time τ_e . It has been established that the two-fluid formalism is valid provided that $St \leq 0.3$ [11]. For larger St , the particles become increasingly uncorrelated with the fluid, and in turn, with one another. When this occurs, the continuum treatment is no longer appropriate.

Using the two-fluid formalism, we recently explored preferential concentration in the context of the particle-induced convective instability [7]. Our model setup consisted of a carrier fluid with an assumed stable temperature gradient, to which a layer of small and dense inertial particles was added to create linearly unstable initial conditions. We restricted our study to particles with $St \leq 0.3$ in order to stay within the limit of validity of the two-fluid model. In addition, due to the high computational cost required to resolve fine particle structures, we primarily ran 2D Direct Numerical Simulations (DNSs). In all cases, we ran the simulations long enough to study the development of the Rayleigh-Taylor instability, and measured the maximum and typical particle concentration enhancement above the horizontally-averaged particle density.

Most notably, we found that the maximum particle concentration enhancement above the mean is related to the particle stopping time τ_p , the rms fluid velocity in the turbulent layer

u_{rms} , and the assumed particle diffusivity κ_p , scaling as $u_{rms}^2 \tau_p / \kappa_p$. Additionally, we showed that the typical particle concentration enhancement over the mean scales as $(u_{rms}^2 \tau_p / \kappa_p)^{1/2}$. We also computed the probability distribution function (pdf) of the particle concentration enhancement above the mean and found that in the presence of inertial particles, the tail of the pdf appears to be an exponential whose slope scales as $(u_{rms}^2 \tau_p / \kappa_p)^{-1/2}$. We then explained the importance of the parameter group $u_{rms}^2 \tau_p / \kappa_p$ using arguments of dominant balance between the inertial concentration and diffusion terms in the particle transport equation (more details can be found in Section IV). Although we showed that the model was quite useful in predicting the maximum particle concentration in turbulent flows, our study was limited to flows where the turbulence was driven by the particles themselves. Therefore, whether these results are more generally applicable to any turbulent particle-laden flow remained to be established. This crucial question is answered in the present paper.

The paper is organized as follows. In Section II we introduce the model setup and the governing equations based on the two-fluid formalism. In Section III we present DNSs for varying governing parameters (such as the Stokes number and the fluid Reynolds number, for instance), and explore how they affect both preferential concentration and the energetics of the system. In Section IV we briefly review the predictive model for maximum particle concentration enhancement presented in [7] and compare it to the new DNSs. We further look at the typical particle concentration enhancement and the associated pdf of the particle concentration. Section V briefly summarizes and presents applications of our model. We discuss the implications of these results and conclude with final remarks.

II. THE MODEL

In this work we use the two-fluid model described in Nasab and Garaud [7] to study the dynamics of a dilute suspension of particles in a turbulent carrier fluid. For simplicity, we assume that the inertial particles have a solid density that is much larger than the mean fluid density such that $\rho_s \gg \rho_f$. We also assume that they are sufficiently small so that Stokes' law can be applied, in which case $\tau_p = \rho_s d_p^2 / 18 \rho_f \nu$, where d_p is the diameter of the particle, ρ_f and ν are the mean density and the kinematic viscosity of the fluid, respectively. Since the particles are much denser than the fluid, effects incorporated in terms such as the

Basset history, Faxen correction, and added mass can be neglected [12]. We additionally require that the particle stopping time τ_p should be much smaller than the typical eddy turnover time of the carrier fluid τ_e , so $St \ll 1$.

We use the Boussinesq approximation [13] for the carrier fluid and obtain the following governing equations after a suitable approximation of the particle equations (see Nasab and Garaud [7]):

$$\frac{\partial \mathbf{u}}{\partial t} + \mathbf{u} \cdot \nabla \mathbf{u} = -\nabla p + r \frac{\mathbf{u}_p - \mathbf{u}}{\tau_p} + \nu \nabla^2 \mathbf{u} + \frac{1}{\rho_f} \mathbf{F}, \quad (1)$$

$$\frac{\partial \mathbf{u}_p}{\partial t} + \mathbf{u}_p \cdot \nabla \mathbf{u}_p = \frac{\mathbf{u} - \mathbf{u}_p}{\tau_p} + \nu_p \nabla^2 \mathbf{u}_p, \quad (2)$$

$$\frac{\partial r}{\partial t} + \nabla \cdot (\mathbf{u}_p r) = \kappa_p \nabla^2 r, \quad (3)$$

$$\nabla \cdot \mathbf{u} = 0, \quad (4)$$

where the fluid velocity is $\mathbf{u} = (u, v, w)$, p is the pressure, and the particle velocity is $\mathbf{u}_p = (u_p, v_p, w_p)$. Within this formalism, we define the local number density of particles to be n_p , and the corresponding mass density to be $\rho_p = n_p m_p$, where m_p is the mass of a single particle. For convenience, we refer to $r = \rho_p / \rho_f$ as the rescaled particle density with respect to the mean density of the carrier fluid (see Nasab and Garaud [7] for details).

By treating the particles as a continuum, we need to account for the stochastic aspect of particle trajectories, such as Brownian motion and the interaction of a particle with its own or another particle's wake. Generally these interactions are complex in nature, and thus, difficult to implement realistically and numerically. Here for simplicity, we assume that they take the form of a diffusion operator in the equations for the particle density and velocity and set the corresponding diffusivities ν_p and κ_p to be constant. This approximation is valid in the limit where Brownian motion is dominant.

In this work, we drive the turbulence mechanically, by forcing the flow to be shear-unstable. We drive the mean flow using a body force given by $\mathbf{F} = F_0 \sin(k_s z) \hat{\mathbf{e}}_x$, where F_0 is the forcing amplitude and $k_s = 2\pi/L_z$ is the wavenumber corresponding to the domain height L_z . By selecting a non-cubic domain (where $L_x > L_z$), the Kolmogorov flow thus generated is linearly unstable for large enough Reynolds number [14].

We initialize the particles with a uniform distribution in r such that $r = r_0$ everywhere in the domain. In this study, we choose to explore the range $0.1 \leq r_0 \leq 10$. Note that $r_0 = \Phi_0 \rho_s / \rho_f$, where the initial volume fraction of the particles Φ_0 is small so that the

system is well within the dilute limit. Smaller values of r_0 correspond to systems such that $\rho_s/\rho_f \lesssim O(1)$. In this case, particle settling due to gravity is negligible, and can thus be ignored. Larger values of $r_0 > 1$ can be obtained when $\rho_s \gg \rho_f$, such as is the case for aerosols or dust in accretion disks. However, particle settling should in principle be taken into account in that limit. Therefore for simplicity, we omit gravity from the particle momentum equation (2) to avoid the effect of settling on the dynamics of the system.

A. Nondimensionalization

In what follows, we define the characteristic length and velocity scales to be

$$L_c = \frac{1}{k_s} = \frac{L_z}{2\pi} \quad \text{and} \quad U_c = \left(\frac{L_z F_0}{2\pi \rho_f} \right)^{1/2}, \quad (5)$$

and by construction, the typical eddy turnover time is

$$\tau_c = \left(\frac{L_z \rho_f}{2\pi F_0} \right)^{1/2}. \quad (6)$$

This choice effectively assumes a balance in the carrier fluid momentum equation between the inertial terms and the forcing, such that $\mathbf{u} \cdot \nabla \mathbf{u} \sim F_0/\rho_f$. After using (5) and (6) to scale Eqs. (1)-(4), the nondimensional governing equations are

$$\frac{\partial \hat{\mathbf{u}}}{\partial t} + \hat{\mathbf{u}} \cdot \nabla \hat{\mathbf{u}} = -\nabla \hat{p} + r_0 \hat{r} \frac{\hat{\mathbf{u}}_p - \hat{\mathbf{u}}}{T_p} + \frac{1}{Re} \nabla^2 \hat{\mathbf{u}} + \sin(z) \hat{\mathbf{e}}_x, \quad (7)$$

$$\frac{\partial \hat{\mathbf{u}}_p}{\partial t} + \hat{\mathbf{u}}_p \cdot \nabla \hat{\mathbf{u}}_p = \frac{\hat{\mathbf{u}} - \hat{\mathbf{u}}_p}{T_p} + \frac{1}{Re_p} \nabla^2 \hat{\mathbf{u}}_p, \quad (8)$$

$$\frac{\partial \hat{r}}{\partial t} + \nabla \cdot (\hat{\mathbf{u}}_p \hat{r}) = \frac{1}{Pe_p} \nabla^2 \hat{r}, \quad (9)$$

$$\nabla \cdot \hat{\mathbf{u}} = 0, \quad (10)$$

where the hatted quantities (as well as the independent variables) are now nondimensional, where $\hat{r} = r/r_0$, and where

$$T_p = \frac{\tau_p}{\tau_c} \quad (11)$$

is the nondimensional stopping time, which can be viewed as a first estimate of the Stokes number. Additionally, the diffusion terms are now characterized by a Reynolds number for the fluid Re , a Reynolds number for the particles Re_p , and the particle Péclet number Pe_p respectively defined by

$$Re = \frac{U_c L_c}{\nu}, \quad Re_p = \frac{U_c L_c}{\nu_p}, \quad Pe_p = \frac{U_c L_c}{\kappa_p}. \quad (12)$$

III. NUMERICAL SIMULATIONS

A. The PADDI-2F code

We use Direct Numerical Simulations to investigate the effects of preferential concentration in the model described in Section II. We use a modified version of the pseudospectral PADDI code, which was originally developed to study double-diffusive phenomena in oceanic contexts [15–17], and later extended to astrophysical applications [18, 19] and to particle-laden flows [7]. PADDI-2F solves the governing equations (7)-(10) in spectral space. Specifically, diffusion terms are treated implicitly in spectral space, whereas both nonlinear and drag terms are first computed in real space, transformed into spectral space, and then, integrated explicitly using a third-order Adams-Bashforth backward-differencing scheme. Drag terms are computed in a way that ensures the total momentum is conserved (other than the dissipation terms) throughout the simulations.

The computational domain is triply-periodic, with $(L_x, L_y, L_z) = (4\pi, 2\pi, 2\pi)$ to ensure that the flow is linearly unstable under the selected forcing. All simulations are run until a statistically steady state has been reached, either starting from the initial conditions as described in Section II, or starting from the end of another simulation at nearby parameters. Due to the high cost of running simulations in 3D and the resolution needed to resolve fine-scale particle structures, we restrict our simulations to $Re \leq 600$ and up to moderate values of $T_p \leq 0.03$ in which the two-fluid formalism is valid. Specifications of all simulations are listed in Table I.

B. The effect of Re on turbulence

We first look at the influence of Re on the turbulence in the absence of particles, which will be used as a reference point for later simulations with particles. We therefore only use the momentum equation (7) and the divergence-free condition (10), and set $r_0 = 0$. We set the resolution of the 3D runs to be $768 \times 384 \times 384$ equivalent grid points in the x -, y -, and z -directions, respectively.

We examine the power spectra of the fluid velocity field once the system has reached a statistically steady state, and compare the results for different Reynolds numbers. We define

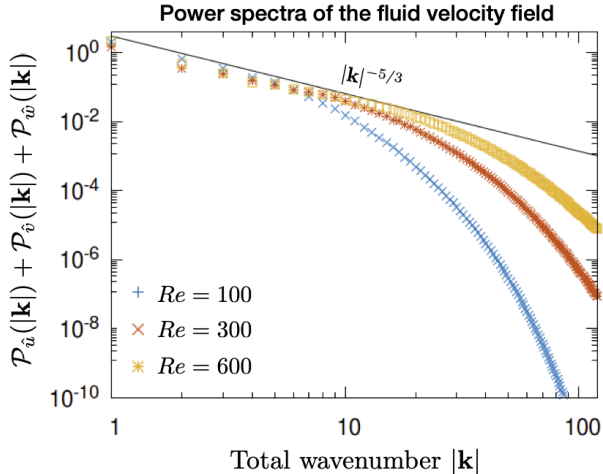


FIG. 1. Instantaneous power spectra of the total fluid velocity field as function of $|\mathbf{k}|$ for simulations in the absence of particles for $Re = 100, 300,$ and 600 . The black solid line scales as $|\mathbf{k}|^{-5/3}$.

the power in mode \mathbf{k} for a scalar quantity $\hat{\xi}$ (e.g. \hat{u}, \hat{v} , and \hat{w}) as

$$P_{\hat{\xi}}(\mathbf{k}, t) = \tilde{\xi}(\mathbf{k}, t)\tilde{\xi}^*(\mathbf{k}, t) \quad (13)$$

where $\mathbf{k} = (k_x, k_y, k_z)$ is the wavevector and $\tilde{\xi}(\mathbf{k}, t)$ and $\tilde{\xi}^*(\mathbf{k}, t)$ are the Fourier transform of $\hat{\xi}$ and its complex conjugate, respectively. For Figures 1, 3, 4, 5, and 7 we present the power spectra $\mathcal{P}_{\hat{\xi}}(|\mathbf{k}|, t)$ as a function of the total wavenumber $|\mathbf{k}| = (k_x^2 + k_y^2 + k_z^2)^{1/2}$, where $\mathcal{P}_{\hat{\xi}}(|\mathbf{k}|, t)$ is the power contained in all the modes whose amplitudes lie between $|\mathbf{k}|$ and $|\mathbf{k}| + 1$.

Figure 1 presents the power spectra of the total fluid velocity field $\mathcal{P}_{\hat{u}}(|\mathbf{k}|) + \mathcal{P}_{\hat{v}}(|\mathbf{k}|) + \mathcal{P}_{\hat{w}}(|\mathbf{k}|)$ extracted at an instant in time after the system has reached a statistically steady state for three simulations with $Re = 100, 300,$ and 600 , respectively. For sufficiently large Re , the system exhibits a well-known energy cascade whose inertial range scales as $|\mathbf{k}|^{-5/3}$, shown here by the black line for ease of comparison. As expected, we find that the inertial range increases with Re and ends at the Taylor microscale $\lambda = \sqrt{15}Re^{-1/2}L_z$. This corresponds to $k_\lambda = 2\pi/\lambda$, which is equal to $k_\lambda \approx 2.6$ for $Re = 100$, $k_\lambda \approx 4.5$ for $Re = 300$, and $k_\lambda \approx 6.3$ for $Re = 600$. In geophysical and astrophysical applications, Re is much larger, with an established inertial range spanning many orders of magnitude, which we do not see for the simulations presented here. Therefore, one must be careful about extrapolating the results obtained in this paper to systems with $Re \gg 10^3$ (see Section V B for more details).

C. The effect of T_p on preferential concentration

We now explore how the other input parameters affect preferential concentration, and how this in turn alters the energetics of the system. We first look at how the non-dimensional stopping time, which is also a proxy for the Stokes number of the particles, affects the system by comparing a 3D simulation with a very low $T_p = 0.005$ to another at a higher $T_p = 0.03$. To do so, we use the PADDI-2F code using Eqs. (7)–(10), with the remaining parameters set as $r_0 = 0.1$, $Re = 100$, $Re_p = 600$, and $Pe_p = 600$. The resolution and domain size for the simulations are set to $768 \times 384 \times 384$ equivalent grid points, and as before, $L_x = 4\pi$ and $L_y = L_z = 2\pi$ (see Table I for more details).

We present snapshots in Figure 2 of the particle concentration field after the system has reached a statistically steady state. In the volume renderings shown in Figures 2(a) and 2(b), we highlight areas of relatively higher particle concentration in red. Both simulations consist of sheet-like particle structures which appear to be about the same size, but denser for the high T_p case. We can see the particle structures in more detail in Figures 2(c) and 2(d), which show the particle concentration deviation from the mean (namely, $\hat{r} - 1$) in a slice taken at $y = 0$. We clearly see that the denser particle structures indeed appear to be the same size for both simulations. The densest structures for the high T_p case have values of $\hat{r} - 1 \approx 3$ compared to $\hat{r} - 1 \approx 0.5$ for structures found in the low T_p case.

The fact that preferential concentration is more efficient at higher values of T_p recovers the well-known results of [1], which are expressed as follows in the two-fluid formalism. Using the particle momentum equation (9), we can express $\hat{\mathbf{u}}_p$ in terms of $\hat{\mathbf{u}}$ and T_p using an asymptotic expansion in T_p :

$$\hat{\mathbf{u}}_p = \hat{\mathbf{u}} - T_p \left(\hat{\mathbf{u}} \cdot \nabla \hat{\mathbf{u}} + \frac{\partial \hat{\mathbf{u}}}{\partial t} - \frac{1}{Re_p} \nabla^2 \hat{\mathbf{u}} \right) + O(T_p^2). \quad (14)$$

Taking the divergence of (14), we then obtain

$$\nabla \cdot \hat{\mathbf{u}}_p = -T_p \nabla \cdot (\hat{\mathbf{u}} \cdot \nabla \hat{\mathbf{u}}) + O(T_p^2), \quad (15)$$

which shows that $\nabla \cdot \hat{\mathbf{u}}_p$ is non zero even though $\nabla \cdot \hat{\mathbf{u}} = 0$, and furthermore depends linearly on T_p for small T_p . It is easy to see (from Eq. 9) that the particle concentration grows (or decays) exponentially since

$$\frac{\partial \hat{r}}{\partial t} = -\hat{r}(\nabla \cdot \hat{\mathbf{u}}_p) + \dots, \quad (16)$$

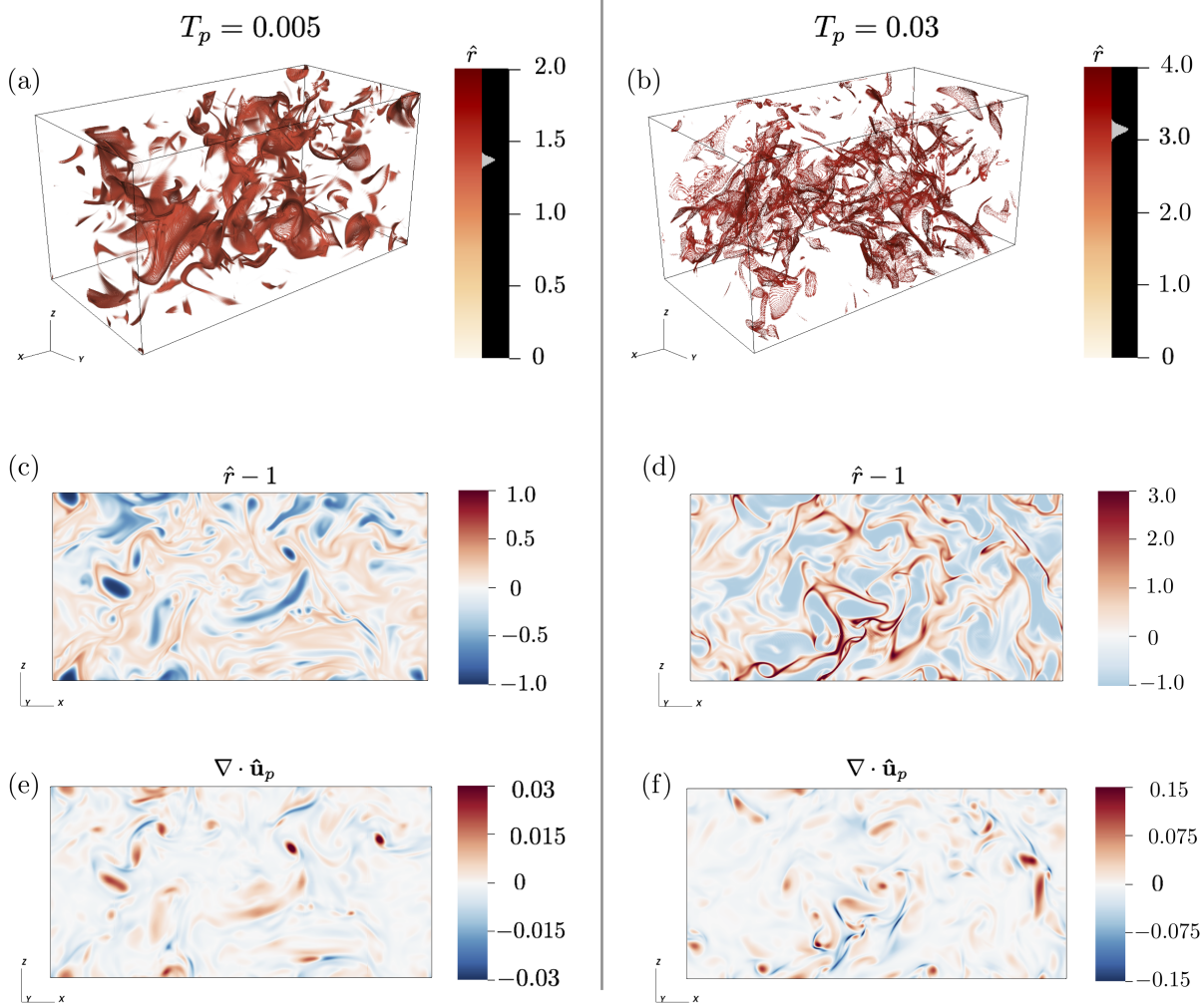


FIG. 2. Comparison of particle concentration snapshots for low $T_p = 0.005$ (left column) and high $T_p = 0.03$ (right column) simulations. Each snapshot was extracted once the system has reached a statistically steady state. (a)-(b): volume rendering of \hat{r} ; (c)-(d): snapshots of the particle concentration enhancement $\hat{r} - 1$ at $y = 0$; (e)-(f): snapshots of $\nabla \cdot \hat{\mathbf{u}}_p$ at $y = 0$. The remaining parameters are: $r_0 = 0.1$, $Re = 100$, $Re_p = 600$, $Pe_p = 600$.

showing that the growth or decay rate of \hat{r} is given by $|\nabla \cdot \hat{\mathbf{u}}_p|$. Figure 2 compares the particle concentration enhancement $\hat{r} - 1$ (panels 2(c) and 2(d)) to the value of $\nabla \cdot \hat{\mathbf{u}}_p$ (panels 2(e) and 2(f)) at the same time. We see that areas where $\nabla \cdot \hat{\mathbf{u}}_p < 0$ (shown in blue) correspond to regions where $\hat{r} - 1$ is maximal, while regions with $\nabla \cdot \hat{\mathbf{u}}_p > 0$ (shown in red) correspond to regions where \hat{r} is close to 0 (equivalently, $\hat{r} - 1$ is close to -1), as expected from the argument above.

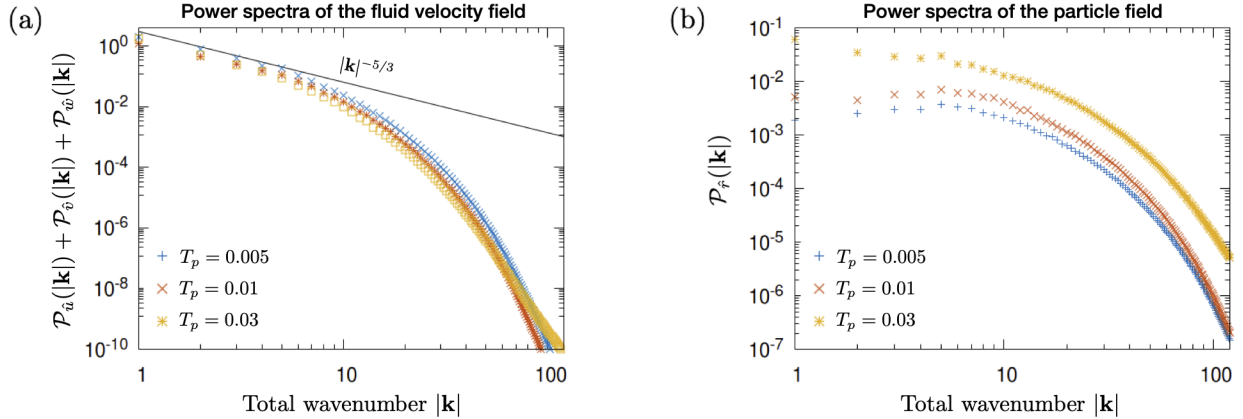


FIG. 3. Instantaneous power spectra of (a) the total fluid velocity field and (b) the particle concentration field as a function of the total wavenumber $|\mathbf{k}|$ for varying T_p . The remaining parameters are $r_0 = 0.1$, $Re = 100$, $Re_p = 600$, and $Pe_p = 600$.

We next compare the power spectra (using Eq. 13) of the particle concentration and fluid velocity fields for simulations with varying T_p , with the remaining parameters fixed as $r_0 = 0.1$, $Re = 100$, $Re_p = 600$ and $Pe_p = 600$. Figure 3(a) shows the power spectrum of the total fluid velocity field $\mathcal{P}_u(|\mathbf{k}|) + \mathcal{P}_v(|\mathbf{k}|) + \mathcal{P}_w(|\mathbf{k}|)$. The solid black line represents the Kolmogorov spectrum given by $|\mathbf{k}|^{-5/3}$. Although there is a subtle decrease in power across all scales for larger T_p , the velocity spectrum appears to be overall unaffected.

Figure 3(b) shows the power spectrum of the particle concentration $\mathcal{P}_{\hat{r}}(|\mathbf{k}|)$. We see that increasing T_p causes an increase in $\mathcal{P}_{\hat{r}}(|\mathbf{k}|)$ at all scales, with the exception of the $\mathbf{k} = \mathbf{0}$ mode whose amplitude instead decreases (not shown here). This is consistent with our expectation that increasing inertia causes an increase in preferential concentration, and is directly related to the snapshots in Figure 2: comparable-sized particle structures are denser (higher \hat{r}) for large T_p than for small T_p .

D. The effect of r_0 on preferential concentration

We next look at the effect of the particle mass loading fraction r_0 on the energetics of the system. We set $T_p = 0.01$, $Re = 100$, $Re_p = 600$, and $Pe_p = 600$ (see Table I for more details) and present the power spectra of the particle concentration and total fluid velocity fields (using Eq. 13) in Figures 4(a) and 4(b), respectively.

Turning first to the power spectrum of the velocity field in Figure 4(a), we see that r_0 has a strong effect on the total energy of the turbulent flow (or equivalently, on the normalization of the power spectrum). The inertial range still shows the usual $|\mathbf{k}|^{-5/3}$ power law, and ends around $k_\lambda \approx 2.6$ in all three simulations, which is the same as the case without particles ($r_0 = 0$ with $Re = 100, Re_p = 600, Pe_p = 600$ in Figure 1). In order to understand why increasing r_0 reduces the turbulent energy, note that in a statistically stationary state, the momentum equation (1) reaches a balance between the inertial terms and body force terms, expressed dimensionally as $\rho_f(\mathbf{u} \cdot \nabla \mathbf{u}) \sim \mathbf{F}$. With the addition of particles that are well-coupled to the fluid, the dominant balance becomes $(\rho_f + \rho_p)(\mathbf{u} \cdot \nabla \mathbf{u}) \sim \mathbf{F}$. In the nondimensionalization presented in Section II A, this balance implies $(1 + r_0)\hat{\mathbf{u}}^2 \simeq O(1)$. With this in mind, we can then expect that $\mathcal{P}_{\hat{u}}(|\mathbf{k}|) + \mathcal{P}_{\hat{v}}(|\mathbf{k}|) + \mathcal{P}_{\hat{w}}(|\mathbf{k}|)$ ought to scale like $1/(1 + r_0)$ at the injection scale. The scaling is confirmed in Figure 4 for $r_0 = 0.1, r_0 = 1$, and $r_0 = 10$ given by the solid, dashed, and dotted lines, respectively.

Figure 4(b) shows the power spectrum of the particle concentration field $\mathcal{P}_{\hat{r}}(|\mathbf{k}|)$, and we see that larger r_0 corresponds to smaller $\mathcal{P}_{\hat{r}}(|\mathbf{k}|)$ across all scales (except the $\mathbf{k} = \mathbf{0}$ mode which is not shown). This is consistent with the fact that larger r_0 results in a decrease in the turbulence intensity (and therefore preferential concentration) across all scales, as observed from the velocity power spectrum.

E. The effect of Re on preferential concentration

In this section, we investigate how varying the fluid Reynolds number affects the energetics, while fixing the other parameters to be $T_p = 0.01, r_0 = 0.1, Re_p = 600$, and $Pe_p = 600$ (see Table I for more details). Figures 5(a) and 5(b) show the power spectra of the total fluid velocity and particle concentration fields, respectively (using Eq. (13)).

In Figure 5(a), the velocity spectra shown are more or less indistinguishable from those of the corresponding fluid-only simulations presented in Section III B. This is not surprising since the value of $r_0 = 0.1$ chosen for these simulations is quite small. Because a larger Re extends the Kolmogorov cascade, finer scales of turbulence are generated. Consequently in Figure 5(b), we also see substantially more power in the particle density field at smaller scales when Re increases. This is also confirmed in the snapshots of the particle concentration enhancement $(\hat{r} - 1)$ shown in Figure 6, which compare simulations with $Re = 100$ and

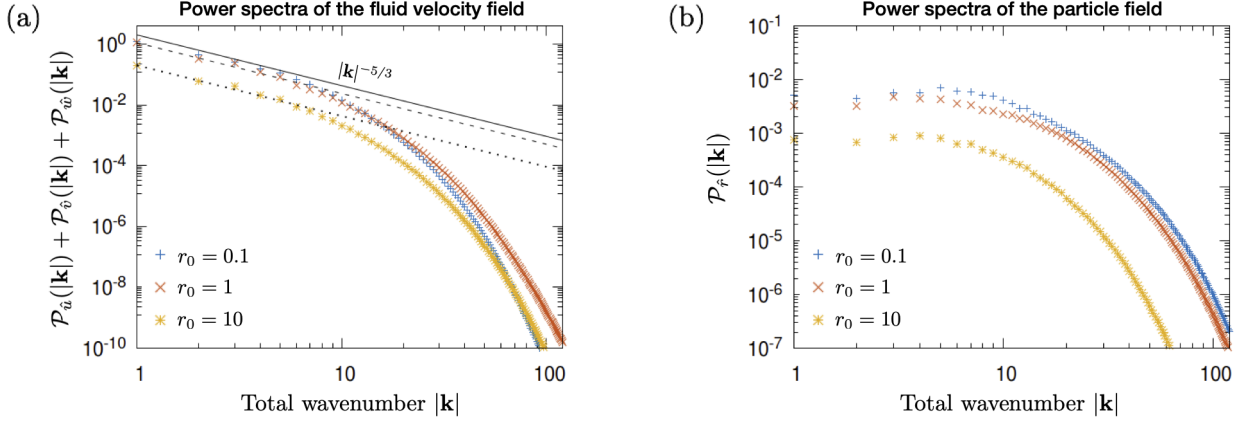


FIG. 4. Instantaneous power spectra of (a) the total fluid velocity field and (b) the particle concentration field as a function of the total wavenumber $|\mathbf{k}|$ for varying r_0 . The remaining parameters are $T_p = 0.01$, $Re = 100$, $Re_p = 600$, and $Pe_p = 600$. The solid, dashed, and dotted lines represents the predicted scaling for the power at the injection scale for $r_0 = 0.1, 1$, and 10 , respectively (see main text for details).

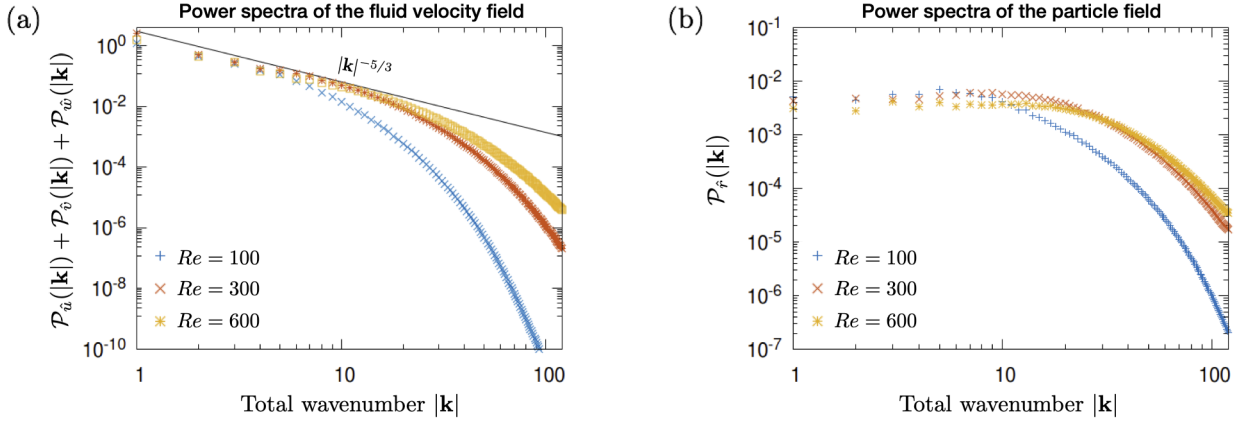


FIG. 5. Instantaneous power spectra of (a) the total fluid velocity field and (b) the particle concentration field as a function of the total wavenumber $|\mathbf{k}|$ for varying Re . The remaining parameters are $T_p = 0.01$, $r_0 = 0.1$, $Re_p = 600$, and $Pe_p = 600$.

$Re = 600$. The finer scales of turbulence for larger Re cause the denser particle structures to appear overall more fragmented and convoluted. On the other hand, we note that the densest filamentary regions (shown in dark red) have comparable thickness for varying Re .

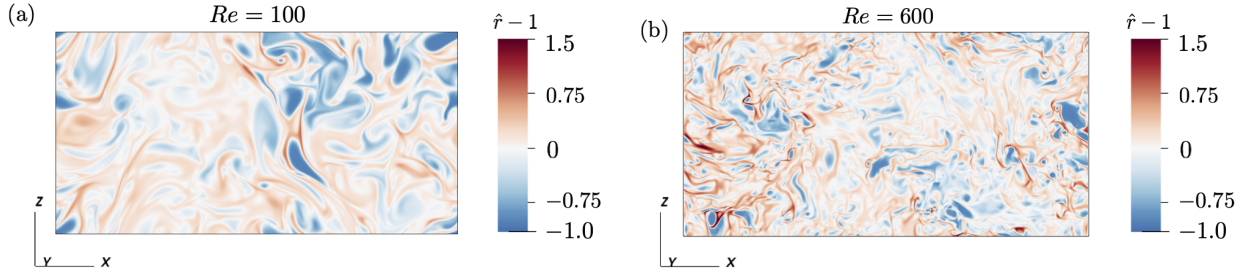


FIG. 6. Snapshots of the particle concentration enhancement above the mean $\hat{r} - 1$ for two different simulations with $Re = 100$ and $Re = 600$. The remaining parameters are $T_p = 0.01$, $r_0 = 0.1$, $Re_p = 600$, and $Pe_p = 600$.

F. The effect of Pe_p and Re_p on preferential concentration

Finally, we examine how the particle diffusion coefficients Pe_p and Re_p affect the energetics of the system. As described in Section II, the particle concentration and momentum diffusivities are necessary when modeling the particles as a continuum, but their origin is grounded in the notion that the particle velocities have a stochastic component in addition to the mean $\hat{\mathbf{u}}_p$. Since the origin of the particle diffusivity is likely the same as that of the momentum diffusivity, we may expect Pe_p and Re_p to be related, and close to one another. In what follows, we take $Pe_p = Re_p$ for simplicity.

Figure 7 shows the power spectra of the particle concentration field and the total fluid velocity field. In Figure 7(b), we see that a larger Pe_p (equivalently, a lower particle diffusivity) results in significantly larger $\mathcal{P}_{\hat{r}}(|\mathbf{k}|)$ across all scales, and thus, the presence of smaller-scale structures in the particle concentration field. By contrast, we see in Figure 7(a) that Pe_p does not affect the velocity power spectrum significantly, other than a slight decrease in energy across all scales for larger Pe_p .

G. Quantifying particle concentration enhancement

In what follows, we quantify particle concentration enhancement by first defining several terms:

$$\hat{r}_{sup}(t) = \max_{\mathbf{x}} \hat{r}(\mathbf{x}, t) \quad (17)$$

Symbol	T_p	r_0	Re	Pe_p	\hat{r}_{sup}	\hat{r}_{rms}	\hat{U}_{rms}	b
–	–	–	100	–	–	–	2.42 ± 0.05	–
–	–	–	300	–	–	–	2.43 ± 0.16	–
–	–	–	600	–	–	–	2.50 ± 0.18	–
●	0.005	0.1	100	1000	2.04 ± 0.11	0.23 ± 0.005	2.17 ± 0.08	10.92 ± 0.18
●	0.005	0.1	100	600	1.92 ± 0.11	0.22 ± 0.01	2.28 ± 0.07	18.04 ± 0.05
●	0.005	0.1	600	1000	3.84 ± 0.43	0.29 ± 0.01	2.26 ± 0.08	8.14 ± 0.01
▲	0.005	1	600	1000	2.35 ± 0.18	0.21 ± 0.01	1.80 ± 0.09	14.79 ± 0.03
■	0.005	10	600	1000	1.27 ± 0.03	0.06 ± 0.004	0.71 ± 0.01	51.72 ± 0.85
○	0.01	0.1	100	100	1.85 ± 0.18	0.22 ± 0.03	2.20 ± 0.06	13.65 ± 0.05
○	0.01	0.1	100	300	2.56 ± 0.35	0.31 ± 0.03	2.20 ± 0.09	9.25 ± 0.01
○	0.01	0.1	100	600	3.17 ± 0.36	0.37 ± 0.03	2.22 ± 0.025	10.18 ± 0.01
○	0.01	0.1	300	600	5.61 ± 1.21	0.41 ± 0.014	2.31 ± 0.07	5.58 ± 0.004
●	0.01	0.1	600	600	6.36 ± 1.14	0.40 ± 0.01	2.16 ± 0.056	5.52 ± 0.007
▲	0.01	1	100	1000	2.40 ± 0.27	0.23 ± 0.02	1.58 ± 0.025	11.60 ± 0.025
△	0.01	1	100	600	2.10 ± 0.17	0.23 ± 0.01	1.63 ± 0.02	13.96 ± 0.03
▲	0.01	1	600	600	2.93 ± 0.22	0.26 ± 0.01	1.69 ± 0.02	9.32 ± 0.01
□	0.01	10	100	1000	1.53 ± 0.08	0.10 ± 0.006	0.82 ± 0.05	33.91 ± 0.21
□	0.01	10	100	600	1.31 ± 0.03	0.09 ± 0.002	0.69 ± 0.004	31.77 ± 0.30
■	0.01	10	600	600	1.39 ± 0.05	0.08 ± 0.002	0.69 ± 0.002	45.47 ± 0.48
●	0.03	0.1	100	300	9.81 ± 2.50	0.64 ± 0.03	2.16 ± 0.06	2.50 ± 0.003
●	0.03	0.1	100	600	8.46 ± 1.81	0.61 ± 0.014	2.05 ± 0.07	2.92 ± 0.004
▲	0.03	1	100	1000	6.95 ± 0.81	0.49 ± 0.02	1.57 ± 0.03	3.36 ± 0.01

TABLE I. Characteristics of the numerical simulations. The first column represents the markers for Figures 9, 10, and 12. The second to fifth columns show T_p , r_0 , Re , and Pe_p (where we have set $Re_p = Pe_p$). The sixth to eighth columns show temporally averaged values for \hat{r}_{sup} , \hat{r}_{rms} , and \hat{U}_{rms} once the system has reached a statistically steady state, and the errors represent a standard deviation around the mean. The last column corresponds to the slope b and its standard error of the exponential tail of the pdfs presented in Section IV B. All 3D simulations were run with $(L_x \times L_y \times L_z) = (4\pi \times 2\pi \times 2\pi)$ with the corresponding number of mesh points used in each direction as $(N_x \times N_y \times N_z) = (768 \times 384 \times 384)$.

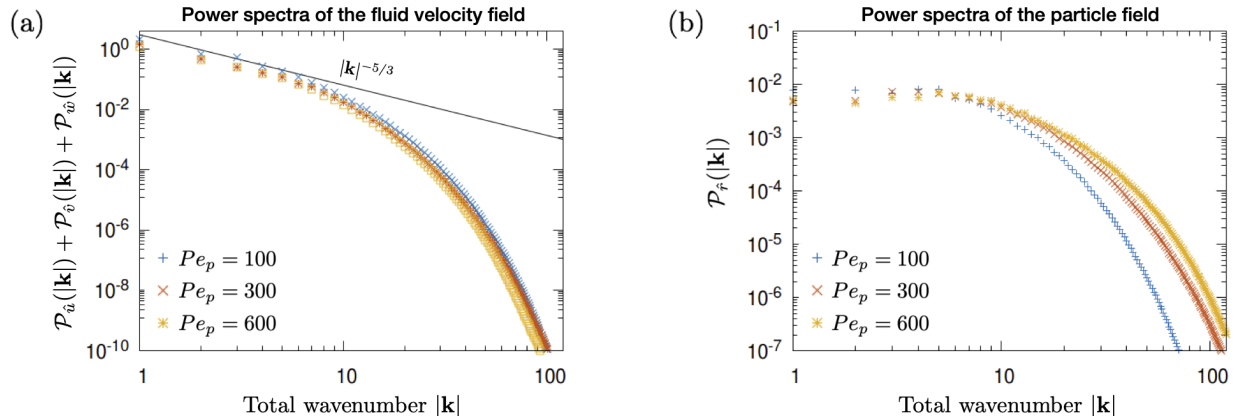


FIG. 7. Instantaneous power spectra of (a) the total fluid velocity field and (b) the particle concentration field as a function of the total wavenumber $|\mathbf{k}|$ for varying Pe_p . The remaining parameters are $T_p = 0.01$, $r_0 = 0.1$, $Re = 100$, and $Re_p = Pe_p$.

representing the maximum particle concentration across the domain,

$$\hat{r}_{rms}(t) = \left[\frac{1}{L_x L_y L_z} \iiint (\hat{r} - 1)^2 dx dy dz \right]^{1/2}, \quad (18)$$

defined as the standard deviation around the mean particle density $\hat{r} = 1$, and the rms fluid velocity defined as

$$\hat{U}_{rms}(t) = \left[\frac{1}{L_x L_y L_z} \iiint [\hat{u}^2(\mathbf{x}, t) + \hat{v}^2(\mathbf{x}, t) + \hat{w}^2(\mathbf{x}, t)] dx dy dz \right]^{1/2}. \quad (19)$$

We first look at how the two measures of particle concentration enhancement defined above, as well as the rms fluid velocity, vary with respect to T_p , r_0 , Re , and Pe_p (assuming as above that $Re_p = Pe_p$). For each simulation presented, we take a temporal average of the quantities defined by Eqs. (17) – (19) after the system has reached a statistically steady state over a time range Δt , and report the means as \hat{r}_{sup} , \hat{r}_{rms} , and \hat{U}_{rms} in Table I. We then take the standard deviation around this temporal average as an estimate of the errorbar (quantifying the variability). Figure 8 presents the temporally averaged values of $\hat{r}_{sup} - 1$, \hat{r}_{rms} , and \hat{U}_{rms} for selected simulations. In Figure 8(a), we present simulations for varying T_p , while holding $r_0 = 0.1$, $Re = 100$, $Re_p = 600$, and $Pe_p = 600$ constant. We see that both $\hat{r}_{sup} - 1$ and \hat{r}_{rms} increase with T_p , while \hat{U}_{rms} is overall unaffected. This is consistent with the observation in Section III C that T_p only has a small effect on the overall power spectrum of the turbulence, but directly controls the rate of preferential concentration. In

Figure 8(b), r_0 is varied, while $T_p = 0.01$, $Re = 100$, $Re_p = 600$, and $Pe_p = 600$ are held constant. We see that all quantities decrease with increasing r_0 . This can be explained by the fact that an increase in r_0 corresponds to a decrease in the turbulent fluid velocity, resulting in a subsequent decrease in the particle concentration enhancement (see Section III D). Moving on to Figure 8(c) where Re is varied while $T_p = 0.01$, $r_0 = 0.1$, $Re_p = 600$, and $Pe_p = 600$ are held constant, we see that \hat{U}_{rms} and \hat{r}_{rms} are overall unchanged, at least within the range of Re shown. In contrast, we see a slight increase of $\hat{r}_{sup} - 1$ with Re . Finally in 8(d), where Pe_p (and Re_p) is varied while $T_p = 0.01$, $r_0 = 0.1$, and $Re = 100$ are held constant, we see that both $\hat{r}_{sup} - 1$ and \hat{r}_{rms} increase with Pe_p , while \hat{U}_{rms} is unchanged (see Section III F). Therefore, we see that the quantities \hat{r}_{sup} , \hat{r}_{rms} , and \hat{U}_{rms} for varying parameters are consistent with the spectra shown in Sections III C-III F.

IV. PREDICTIVE MODEL

As discussed in Section I, Nasab and Garaud [7] found that the maximum particle concentration in a fluid where the turbulence is driven by the particle Rayleigh-Taylor instability scales as $u_{rms}^2 \tau_p / \kappa_p$, and presented theoretical arguments of dominant balance that support this law. For pedagogical purposes, we reproduce the arguments here, and then verify whether the same scaling law applies for particles in mechanically-driven (shear-induced) turbulence as studied in this paper.

We start with the particle concentration equation (9) and substitute $\hat{r} = 1 + \hat{r}'$ to get

$$\frac{\partial \hat{r}'}{\partial t} + (1 + \hat{r}') \nabla \cdot \hat{\mathbf{u}}_p + \hat{\mathbf{u}}_p \cdot \nabla \hat{r}' = \frac{1}{Pe_p} \nabla^2 \hat{r}', \quad (20)$$

where \hat{r}' is the particle concentration enhancement over the mean.

As in Nasab and Garaud [7], we assume that in regions of maximal concentration enhancement there is a dominant balance between the inertial concentration term and the diffusion term expressed as

$$\nabla \cdot \hat{\mathbf{u}}_p \sim \frac{1}{Pe_p} \nabla^2 \hat{r}'. \quad (21)$$

Using Eq. (15) in Eq. (21), we obtain

$$-T_p \nabla \cdot (\hat{\mathbf{u}} \cdot \nabla \hat{\mathbf{u}}) \sim \frac{1}{Pe_p} \nabla^2 \hat{r}'. \quad (22)$$

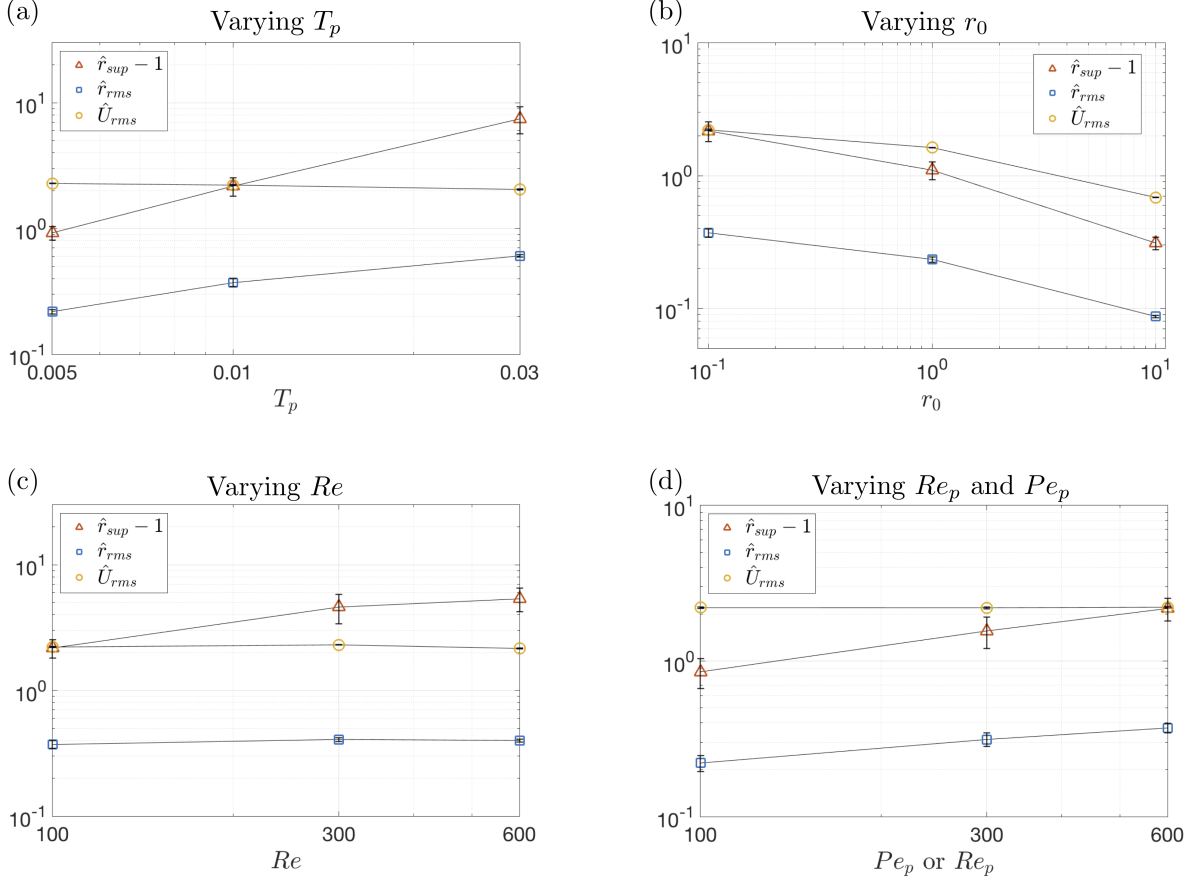


FIG. 8. Temporally averaged maximum and typical particle concentration enhancement ($\hat{r}_{sup} - 1$ and \hat{r}_{rms} , respectively) and the temporally averaged rms fluid velocity \hat{U}_{rms} for (a) varying T_p , (b) varying r_0 , (c) varying Re , and (d) varying Pe_p and Re_p from simulations that have reached a statistically steady state. Error bars represent one standard deviation around the mean. Unless otherwise stated, $T_p = 0.01$, $r_0 = 0.1$, $Re = 100$, $Pe_p = 600$, and $Re_p = 600$ (see main text). More details of the simulations can be found in Table I.

Assuming that the characteristic lengthscale involved in the inertial term and the diffusive term are the same, dimensional analysis reveals that

$$\hat{r}' \sim \hat{U}_{rms}^2 T_p Pe_p, \quad (23)$$

where \hat{U}_{rms} represent the characteristic fluid velocity of the system (see Eq. 19). Dimensionally, this expression becomes

$$\left(\frac{\rho'_p}{\bar{\rho}_p}\right)_{max} \sim \frac{u_{rms}^2 \tau_p}{\kappa_p}, \quad (24)$$

where $\rho'_p = \hat{r}' r_0 \rho_s$ is the local particle density enhancement over the mean $\bar{\rho}_p = r_0 \rho_s$ (see [7] for more details) and u_{rms} is the dimensional rms fluid velocity. We now have a scaling law relating particle concentration enhancement \hat{r}' to only three properties of the flow: the characteristic fluid velocity, the particle stopping time, and the particle diffusivity.

A. Maximum particle concentration enhancement

As in Nasab and Garaud [7], we compare the scaling law (23) to our selected measure of maximum particle concentration enhancement $\hat{r}_{sup} - 1$ (see Eq. 17). In Figure 9, we present $\hat{r}_{sup} - 1$ versus $\hat{U}_{rms}^2 T_p Pe_p$ (with the legend and simulation details found in Table I). Each point corresponds to one simulation, where the values of \hat{r}_{sup} and \hat{U}_{rms} were extracted after the system has reached a statistically steady state. Various marker types represent varying T_p , r_0 , Re , Pe_p , and Re_p : the color represents the value for T_p or Re , the shape represents r_0 , and colored outlines represent Pe_p (or equivalently Re_p , since $Re_p = Pe_p$). The solid line represents the scaling $\hat{r}' \sim \hat{U}_{rms}^2 T_p Pe_p$.

Our main conclusion is that the scaling law proposed by Nasab and Garaud [7] in the context of the particle-driven convective instability also holds more generally in mechanically-driven turbulent flows, which is perhaps not surprising, but needed to be established. As expected, we see points for larger T_p or smaller r_0 have larger \hat{r}_{sup} , while larger r_0 results in a smaller \hat{U}_{rms} , and therefore smaller \hat{r}_{sup} , as discussed in Section III G. We also see that for larger Re , \hat{U}_{rms} increases slightly, resulting in larger \hat{r}_{sup} .

B. Typical particle concentration enhancement

In our previous work [7], we also showed that the typical particle concentration enhancement \hat{r}_{rms} did not follow the scaling law given by Eq. (23), but instead scaled like

$$\hat{r}_{rms} \sim \sqrt{\hat{U}_{rms}^2 T_p Pe_p}, \quad (25)$$

which dimensionally is

$$\left(\frac{\rho'_p}{\bar{\rho}_p} \right)_{rms} \sim \left(\frac{u_{rms}^2 \tau_p}{\kappa_p} \right)^{1/2}. \quad (26)$$

We see that this result also holds for this work in Figure 10. The data points do not follow the scaling law (23) shown by the solid line, and instead follow the dashed line representing

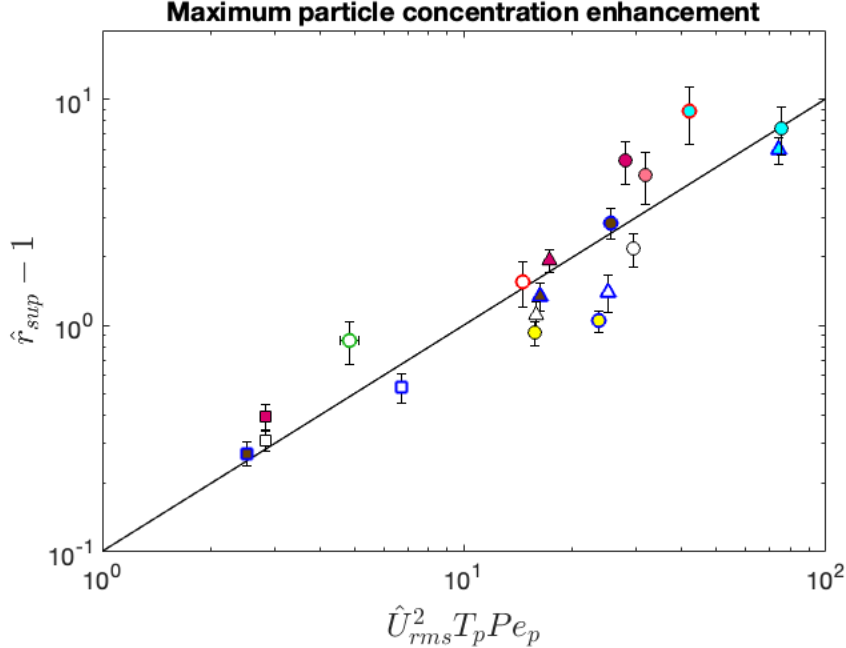


FIG. 9. Maximum particle concentration enhancement over the mean as function of $\hat{U}_{rms}^2 T_p Pe_p$ with varying parameters (i.e. T_p , r_0 , Re , Re_p , and Pe_p). The black solid line represents $\hat{r}_{sup} - 1 = (1/10)\hat{U}_{rms}^2 T_p Pe_p$. The legend and details of simulations can be found in Table I.

$$\hat{r}_{rms} \sim \hat{U}_{rms} \sqrt{T_p Pe_p}.$$

As argued by Nasab and Garaud [7], the fact that \hat{r}_{rms} depends on the same *combination* of parameters as $\hat{r}_{sup} - 1$ (albeit with a different power law) strongly suggests that the entire pdf of the concentration enhancement depends on the combination $\hat{U}_{rms}^2 T_p Pe_p$. To see whether a similar argument applies here, Figure 11 presents pdfs of \hat{r} for selected simulations of varying (a) T_p and (b) r_0 (with simulation details in Table I). These pdfs represent the probability of one pixel in the simulation to have a concentration whose value lies between \hat{r} and $\hat{r} + \Delta\hat{r}$, where $\Delta\hat{r} = 0.002$. The pdf would take the form of a delta function centered on $\hat{r} = 1$ in the absence of preferential concentration ($T_p \rightarrow 0$), since the particle density in that case remains equal to one everywhere and at all times.

On the other hand when preferential concentration is present, the pdf broadens as the particle density becomes more inhomogeneous. We see in Figure 11(a), where T_p is varied while holding $r_0 = 0.1$, $Re = 100$, $Pe_p = 600$, and $Re_p = 600$ constant, that the pdf appears relatively narrow around the mean value $\hat{r} = 1$ for small T_p . As T_p increases, the spatial distribution of the particles becomes more heterogeneous due to preferential concentration,

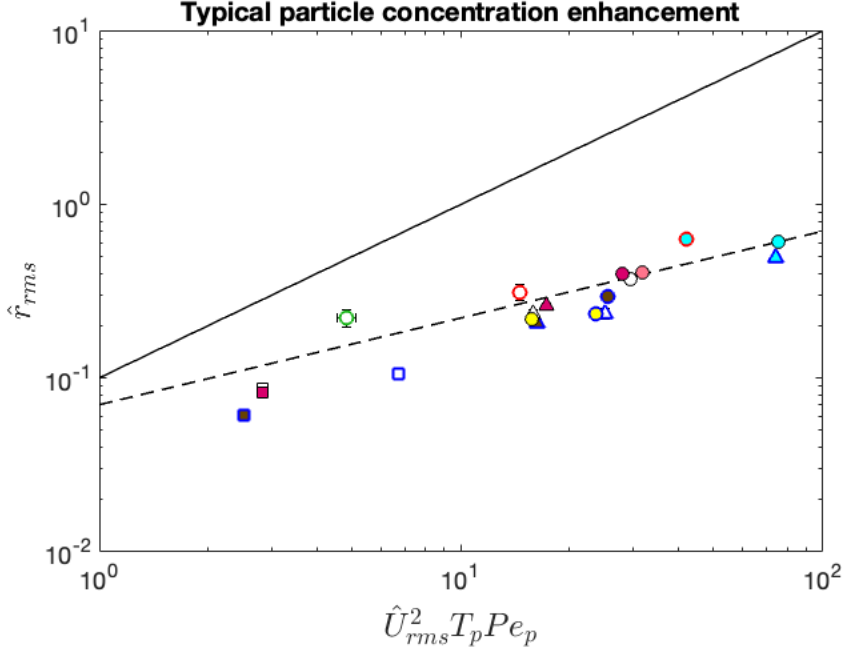


FIG. 10. Typical particle concentration enhancement over the mean as a function of $\hat{U}_{rms}^2 T_p Pe_p$ with varying parameters (i.e. T_p , r_0 , Re , Re_p , and Pe_p). The black dotted line represents $\hat{r}_{rms} = (0.07)\hat{U}_{rms}(T_p Pe_p)^{1/2}$ and the solid line represents $\hat{r}_{rms} = (1/10)\hat{U}_{rms}^2 T_p Pe_p$. The legend and details of simulations can be found in Table I.

and the pdf widens considerably. We also see an increase in the probability of events of no particles (when $\hat{r} \simeq 0$) and the appearance of an elongated tail capturing extreme events where the particle concentration is largest. The tail is exponential, of the form $p(\hat{r}) \propto e^{-b\hat{r}}$ (see Nasab and Garaud [7]).

Moving to Figure 11(b) in which r_0 is varied while $T_p = 0.01$, $Re = 100$, $Pe_p = 600$, and $Re_p = 600$, we see that increasing r_0 causes the pdf to become narrower. This is consistent with the fact that a larger r_0 lowers the amplitude of the turbulence in the system, and consequently, weakens preferential concentration.

Nasab and Garaud [7] studied more quantitatively the exponential tail of the pdf, which seems to be almost ubiquitous, and found that its decay rate b scales as $(\hat{U}_{rms}^2 T_p Pe_p)^{-1/2}$. In Figure 12, we present b as a function of $\hat{U}_{rms}^2 T_p Pe_p$, where b was found by fitting a decaying exponential function to the pdfs presented in Figure 11, along with additional pdfs computed from simulations with varying Re , Pe_p , and Re_p . Each simulation is represented by one data point with the same marker type used in Figures 9 and 10 (with simulation details in Table

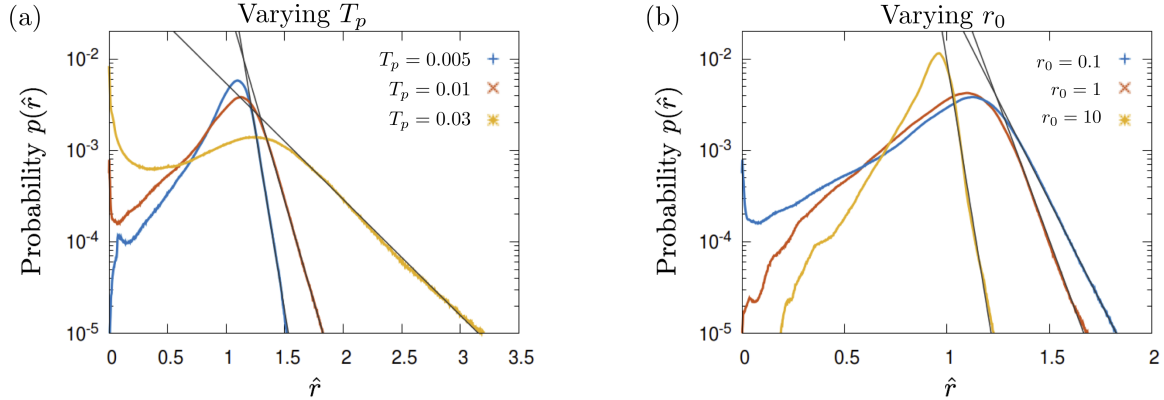


FIG. 11. Probability distribution functions for \hat{r} , computed from simulations that have reached a statistically steady state (a) for varying T_p with $r_0 = 0.1, Re = 100, Pe_p = 600, Re_p = 600$ and (b) for varying r_0 with $T_p = 0.01, Re = 100, Pe_p = 600, Re_p = 600$. The gray lines fit the tail of each pdf and are of the form $p(\hat{r}) \propto e^{-b\hat{r}}$. Values of b and simulation details can be found in Table I.

I), where the errors on b are not shown since they are much smaller than the marker size. The data points appear to follow the blue line given by $(\hat{U}_{rms}^2 T_p Pe_p)^{-1/2}$, consistent with results from Nasab and Garaud [7]. This demonstrates that $\hat{r}_{rms} \sim 1/b$, a result that is not entirely surprising since it would actually be exact if the pdfs were purely exponential.

V. SUMMARY, APPLICATIONS, AND DISCUSSION

A. Summary

In Nasab and Garaud [7] we studied preferential concentration in a two-way coupled particle-laden flow in the context of the particle-driven convective instability. We found that the maximum particle concentration enhancement above the mean scales as $u_{rms}^2 \tau_p / \kappa_p$, where u_{rms} is the rms fluid velocity, τ_p is the particle stopping time, and κ_p is the assumed particle diffusivity. Additionally, we found that the typical particle concentration enhancement over the mean scales as $(u_{rms}^2 \tau_p / \kappa_p)^{1/2}$ and the pdf of the particle concentration over the mean has an exponential tail whose slope scales like $(u_{rms}^2 \tau_p / \kappa_p)^{-1/2}$. However, it was not clear that these results would remain valid in a system in which the turbulence is not driven by the particles themselves. In this work, we confirm that the results of Nasab and Garaud [7] apply in a system in which the turbulence is mechanically-driven. With this extension to a

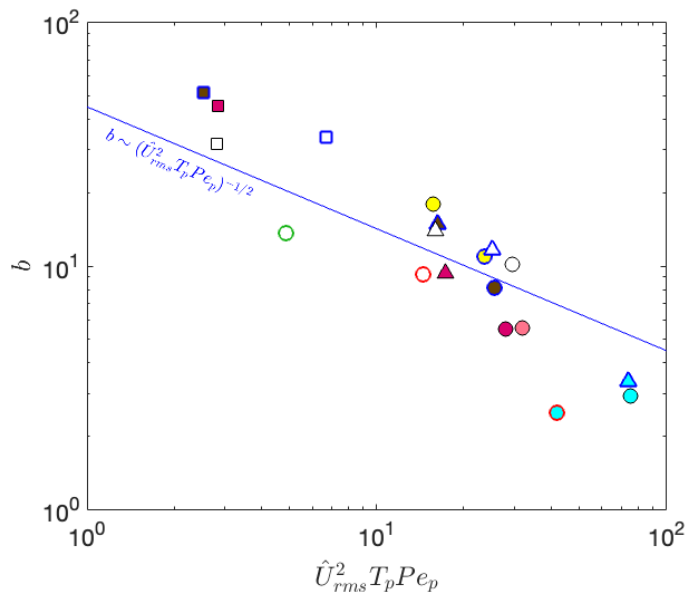


FIG. 12. The slope b of the exponential tail of the pdf of \hat{r} as a function of $\hat{U}_{rms}^2 T_p Pe_p$ for simulations at various T_p , r_0 , Re , Re_p , and Pe_p (where $Re_p = Pe_p$). The blue solid line shows $b \sim (\hat{U}_{rms}^2 T_p Pe_p)^{-1/2}$. See Table I for more details.

much wider class of turbulent systems, our model has important consequences for preferential concentration in the various applications introduced in Section I. In the next sections, we discuss the potential caveats one should bear in mind before applying the model to real physical systems, and present a particular prediction of the model for droplet concentration in clouds.

B. Extension of the model to higher Re

In general, realistic applications of preferential concentration in natural systems take place in environments such as clouds, river outflows, or accretion disks, that are highly turbulent in nature, and whose Reynolds numbers are asymptotically large. Because of this, the velocity spectra have an inertial range which spans many orders of magnitudes in lengthscales. For sufficiently turbulent flows, it is well established that the Stokes number increases with wavenumber and reaches a maximum at the end of the inertial range (i.e. near the Taylor microscale). This poses two problems in terms of the extension of our results to very strongly turbulent flows. On the one hand, it is possible for the Stokes number at the

Taylor microscale to exceed the threshold of validity of the two-fluid approximation (even if $St < 0.3$ at the injection scale). In that case, our results are not expected to apply. On the other hand, even if the two-fluid approximation remains valid, one could question whether our results, which were obtained for moderate Reynolds numbers, still apply when $Re \rightarrow \infty$.

Indeed, due to the high computational cost of running 3D DNSs, we only looked at moderately turbulent systems where $Re \lesssim 600$. In that case, the inertial range of the velocity spectra is quite limited (see Section III). As a result, the characteristic fluid velocity measured at the injection scale is comparable to the corresponding fluid velocity measured at the Taylor microscale. However when $Re \rightarrow \infty$, the velocities at these two scales may be vastly different. This naturally brings up a valid question concerning the predictive model: is the maximum particle concentration enhancement dependent on the fluid velocity measured at the injection scale (as we assumed in this work), or at the Taylor microscale where the Stokes number is maximal? A further look into the data may provide some preliminary clue to the answer (although simulations at much higher Re will ultimately be needed to fully confirm the results).

We saw in Section IV that our predictive model for maximum particle concentration enhancement in the two-fluid approximation depends on the fluid velocity, the particle stopping time, and the assumed particle diffusivity, as

$$\left(\frac{\rho'_p}{\bar{\rho}_p}\right)_{max} \approx \alpha \frac{u^2(\ell)\tau_p}{\kappa_p} \quad (27)$$

for some prefactor α , where here we allow for the possibility that the correct value of u may be different from u_{rms} . We now consider the hypothesis raised above that the fluid velocity may need to be that of the Taylor microscale instead, such that $\ell = \lambda$. Assuming a Kolmogorov spectrum for the kinetic energy, it then follows that

$$u(\lambda) = u_{rms}(\lambda k_s)^{1/3}, \quad (28)$$

where we recall that $2\pi/k_s = L_z$ is the height of the computational domain. Using the fact that $\lambda k_s = \sqrt{15}Re^{-1/2}$ we obtain

$$u(\lambda) = u_{rms}(15)^{1/6}Re^{-1/6}. \quad (29)$$

Substituting $u(\lambda)$ in (27), the maximum particle concentration enhancement in this alternative model would be

$$\left(\frac{\rho'_p}{\bar{\rho}_p}\right)_{max} \sim Re^{-1/3} \frac{u_{rms}^2 \tau_p}{\kappa_p}. \quad (30)$$

This formula suggests that $(\rho'_p/\bar{\rho}_p)_{max}$ should decrease with increasing Re . If this were the case, then we would expect that $(\rho'_p/\bar{\rho}_p)_{max}$ should be approximately twice as large for $Re = 100$ in comparison to $Re = 600$ (with the remaining parameters fixed to be the same). This is contrary to the observations from our simulations, in which we see the opposite trend (see, e.g. Figure 8(c)). We therefore conclude that our original model, in which $(\rho'_p/\bar{\rho}_p)_{max} \sim u_{rms}^2 \tau_p / \kappa_p$, is more likely to be correct. These results, however, will need to be confirmed more directly with simulations at much higher Reynolds number.

C. Application to natural systems

While the question of the applicability of our model to very large Reynolds number systems was partially addressed in the previous section, a second, much more difficult question arises concerning the applicability and validity of the two-fluid equations themselves. In particular, the central result of this work is the role of particle diffusion (κ_p) in controlling the maximum and typical (rms) particle concentration enhancement (see Sec. IV A-IV B), so one may rightfully question whether the diffusion approximation used in Eqs. (1)–(4) is valid in the first place. A complete answer to this question is largely beyond the scope of this paper, and will require either delicate laboratory experiments, or DNSs of a large number of fully-resolved particles interacting with a turbulent fluid.

In the limit where the particles are very small, however, stochastic collisions with the fluid molecules are a source of dispersion in the particle transport equation (usually referred to as Brownian motion), that can be modeled as a diffusion process and whose coefficient is given by

$$\kappa_p \approx \frac{k_B T_m}{6\pi s_p \rho_f \nu}, \quad (31)$$

where $k_B = 1.38 \times 10^{-23} \text{ J} \cdot \text{K}^{-1}$ is the Boltzmann constant, T_m is the mean temperature of the fluid, and s_p is the particle radius. This expression can be considered as a lower limit on the effective particle diffusivity, and using it in conjunction with Eq. (24) and (26), provides an upper limit on the maximum particle concentration $(\rho'_p/\bar{\rho}_p)_{max}$ and the rms particle concentration enhancement $(\rho'_p/\bar{\rho}_p)_{rms}$.

To see what kind of prediction for particle concentration this lower-limit estimate for κ_p leads to, it is helpful to consider a specific application, such as that of rain formation in warm clouds (e.g. cumulus or stratocumulus clouds). In this application, turbulence

is generally mechanically-driven, generated by vertical drafts and wind shear. It has been largely hypothesized that the broadening of the droplet spectrum during the initial stage of droplet growth is due to preferential concentration followed by enhanced collision rates and coalescence [20]. With this in mind, we consider small droplets of radius $s_p = 10 \mu\text{m}$ and density $\rho_s = 1000 \text{ kg/m}^3$ with the typical values for the properties of ambient air being $\rho_f = 1 \text{ kg/m}^3$, $\nu \approx 10^{-5} \text{ m}^2/\text{s}$, and a mean temperature of $T_m \approx 300 \text{ K}$.

Based on these estimates, the stopping time for a cloud droplet is given by

$$\tau_p = \frac{2\rho_s s_p^2}{9\rho_f \nu} \approx (2 \times 10^{-3} \text{ s}) \left(\frac{s_p}{10 \mu\text{m}} \right)^2, \quad (32)$$

and the particle diffusivity due to Brownian motion is given by

$$\kappa_p = (2 \times 10^{-12} \text{ m}^2/\text{s}) \left(\frac{10 \mu\text{m}}{s_p} \right) \left(\frac{T_m}{300 \text{ K}} \right). \quad (33)$$

Using this, we can then obtain an upper limit estimate of the maximum and rms particle concentration enhancements as

$$\left(\frac{\rho'_p}{\bar{\rho}_p} \right)_{max} \lesssim \alpha \frac{u_{rms}^2 \tau_p}{\kappa_p} \approx 10^8 \left(\frac{u_{rms}}{1 \text{ m/s}} \right)^2 \left(\frac{s_p}{10 \mu\text{m}} \right)^2 \left(\frac{2 \times 10^{-12} \text{ m}^2/\text{s}}{\kappa_p} \right) \quad (34)$$

$$\left(\frac{\rho'_p}{\bar{\rho}_p} \right)_{rms} \lesssim \gamma u_{rms} \sqrt{\frac{\tau_p}{\kappa_p}} \approx 2 \times 10^3 \left(\frac{u_{rms}}{1 \text{ m/s}} \right) \left(\frac{s_p}{10 \mu\text{m}} \right) \left(\frac{2 \times 10^{-12} \text{ m}^2/\text{s}}{\kappa_p} \right)^{1/2} \quad (35)$$

where we have used $\alpha \approx 0.1$ and $\gamma \approx 0.07$ extracted from our simulations (see Figures 9 and 10), and a fiducial value of $u_{rms} = 1 \text{ m/s}$ was assumed. This result is quite remarkable, given that the characteristic Stokes number St associated with these droplets is very small. Indeed, assuming that the eddy turnover time is $\tau_e \sim L/u_{rms}$ where $L \sim 1 \text{ km}$ is a typical cloud height, we find that

$$St \simeq \frac{\tau_p}{\tau_e} \approx (2 \times 10^{-6}) \left(\frac{s_p}{10 \mu\text{m}} \right)^2 \left(\frac{1 \text{ km}}{L} \right) \left(\frac{u_{rms}}{1 \text{ m/s}} \right). \quad (36)$$

This suggests that strong preferential concentration is possible even when $St \ll 1$ (a surprising result that is supported by the DNSs presented in Section III).

Of course, as discussed above, this provides only an upper limit estimate of the particle concentration enhancement, which is only valid as long as κ_p is dominated by the effects of Brownian motion. To check whether this is likely true in the cloud application considered, we compute the corresponding volume fraction occupied by the particles in regions of maximal concentration. We find that if the mean liquid water content of the cloud is $\bar{\rho}_p \approx 1$

mg/m^3 , then the average volume fraction occupied by the droplets is $\bar{\Phi} = (\bar{\rho}_p/\rho_s) \approx 10^{-9}$. Thus, the associated maximum and typical volume fraction achievable through preferential concentration are

$$\Phi_{max} \approx \bar{\Phi}(\rho'_p/\bar{\rho}_p)_{max} \approx O(0.1), \quad (37)$$

$$\Phi_{rms} \approx \bar{\Phi}(\rho'_p/\bar{\rho}_p)_{rms} \approx O(10^{-6}). \quad (38)$$

With the possibility of very large volume fractions emerging out of the preferential concentration process, we must therefore account for the possibility that particles may interact hydrodynamically through their wakes, which would increase κ_p (and therefore lower $(\rho'_p/\bar{\rho}_p)_{max}$ and Φ_{max} , and possibly also $(\rho'_p/\bar{\rho}_p)_{rms}$ and Φ_{rms}). For simplicity, we use the results of Segre et al. [21] to construct an effective diffusion coefficient associated with hydrodynamic interactions. They suggest that the mutually-induced dispersion can be modeled by

$$\kappa_p \approx \beta(\Phi)s_pV_p, \quad (39)$$

where β is a function of the volume fraction Φ occupied by the particles and V_p is the velocity of the particles relative to the fluid. Segre et al. [21] found that $\beta(\Phi) \lesssim 0.1$ for volume fractions of up to $\Phi \approx 0.2$. Thus we can construct an approximate upper limit for κ_p by setting $\beta = 0.1$.

The relative velocity of the particles with respect to the fluid is obtained following Maxey [1] (and the arguments presented in Eq. 14) to be

$$V_p = |\mathbf{u}_p - \mathbf{u}| \approx \tau_p \left| \frac{\partial \mathbf{u}}{\partial t} + \mathbf{u} \cdot \nabla \mathbf{u} \right| + O(\tau_p^2). \quad (40)$$

We can estimate it roughly using dimensional arguments as

$$V_p(\ell) \approx \tau_p \frac{u^2(\ell)}{\ell} \approx \tau_p \frac{u_{rms}^2}{L} \left(\frac{\ell}{L} \right)^{-1/3}, \quad (41)$$

assuming a Kolmogorov scaling for the eddy velocity $u(\ell)$ at scale ℓ . We therefore see that V_p will be largest at the Taylor microscale, and set $\ell = \lambda \approx \sqrt{15}Re^{-1/2}L$ to obtain an upper limit for V_p :

$$V_p \lesssim \tau_p \frac{u_{rms}^2}{L} (15)^{-1/6} Re^{1/6}. \quad (42)$$

Using (42) in (39) we can now obtain an upper limit on κ_p , as

$$\kappa_p \lesssim \beta s_p V_p \approx (3 \times 10^{-11} \text{ m}^2/\text{s}) \left(\frac{s_p}{10 \text{ } \mu\text{m}} \right)^3 \left(\frac{u_{rms}}{1 \text{ m/s}} \right)^{13/6} \left(\frac{1 \text{ km}}{L} \right)^{5/6}, \quad (43)$$

which is only about one order of magnitude larger than the value for κ_p obtained by considering the contribution due to Brownian motion only (for Eq. 34).

We apply this formulation for κ_p in (27) and find that

$$\left(\frac{\rho'_p}{\bar{\rho}_p}\right)_{max} \lesssim \alpha \frac{u_{rms}^2 \tau_p}{\kappa_p} \approx 10^7 \left(\frac{u_{rms}}{1 \text{ m/s}}\right)^2 \left(\frac{s_p}{10 \text{ }\mu\text{m}}\right)^2 \left(\frac{3 \times 10^{-11} \text{ m}^2/\text{s}}{\kappa_p}\right), \quad (44)$$

$$\left(\frac{\rho'_p}{\bar{\rho}_p}\right)_{rms} \lesssim \gamma u_{rms} \sqrt{\frac{\tau_p}{\kappa_p}} \approx 600 \left(\frac{u_{rms}}{1 \text{ m/s}}\right) \left(\frac{s_p}{10 \text{ }\mu\text{m}}\right) \left(\frac{3 \times 10^{-11} \text{ m}^2/\text{s}}{\kappa_p}\right)^{1/2}, \quad (45)$$

with a corresponding maximal and rms volume fraction

$$\Phi_{max} \approx \bar{\Phi}(\rho'_p/\bar{\rho}_p)_{max} \approx O(0.01), \quad (46)$$

$$\Phi_{rms} \approx \bar{\Phi}(\rho'_p/\bar{\rho}_p)_{rms} \approx O(10^{-6}). \quad (47)$$

Note that since these were obtained using upper limits on κ_p , they can be viewed as lower limits on Φ_{max} and Φ_{rms} .

Overall, this shows that both lower and upper limit estimates for the particle diffusivity κ_p yield relatively consistent results in the context of cloud applications, and more importantly, that cloud turbulence could produce very large localized enhancements of the droplet concentration, despite the fact that the Stokes number is very low. Applications of this work to dust growth in protoplanetary disks were discussed by Garaud and Nasab [22], with very similar conclusions.

Of course, our results also show that these extreme events where Φ approaches Φ_{max} are rare, belonging to the tail of an exponential distribution. However, it is also well known in the context of both rain formation [3, 4] and planet formation [5, 6], that producing a few larger particles is all it takes for the process to start. Indeed, these larger “lucky particles” then sediment or drift with respect to the smaller ones, and can continue to grow by sweeping the latter. As such, particle growth in these contexts is controlled by what happens in the tail of the particle size distribution, which is why the results discussed here are particularly relevant.

ACKNOWLEDGEMENTS

S. N. is supported by NSF AST-1908338. Simulations were run on a modified version of the PADDI code, originally written by S. Stellmach, on the UCSC Lux cluster and the

NERSC Cori supercomputer. The authors thank Eckart Meiburg for his invaluable insight.

- [1] M. R. Maxey. The gravitational settling of aerosol particles in homogeneous turbulence and random flow fields. *Journal of Fluid Mechanics*, 174:441–465, 1987. doi: 10.1017/S0022112087000193.
- [2] Lian-Ping Wang, Orlando Ayala, Bogdan Rosa, and Wojciech W Grabowski. Turbulent collision efficiency of heavy particles relevant to cloud droplets. *New Journal of Physics*, 10(7): 075013, 2008.
- [3] BJ Devenish, Peter Bartello, J-L Brenguier, LR Collins, Wojciech W Grabowski, RHA IJzermans, Szymon P Malinowski, MW Reeks, JC Vassilicos, L-P Wang, et al. Droplet growth in warm turbulent clouds. *Quarterly Journal of the Royal Meteorological Society*, 138(667): 1401–1429, 2012.
- [4] Wojciech W Grabowski and Lian-Ping Wang. Growth of cloud droplets in a turbulent environment. *Annual review of fluid mechanics*, 45:293–324, 2013.
- [5] T Birnstiel, M Fang, and A Johansen. Dust evolution and the formation of planetesimals. *Space Science Reviews*, 205(1-4):41–75, 2016.
- [6] SJ Weidenschilling and Jeffrey N Cuzzi. Formation of planetesimals in the solar nebula. In *Protostars and planets III*, pages 1031–1060, 1993.
- [7] Sara Nasab and Pascale Garaud. Preferential concentration in the particle-induced convective instability. *Phys. Rev. Fluids*, 5:114308, Nov 2020. doi:10.1103/PhysRevFluids.5.114308. URL <https://link.aps.org/doi/10.1103/PhysRevFluids.5.114308>.
- [8] CT Crowe, TR Troutt, and JN Chung. Numerical models for two-phase turbulent flows. *Annual Review of Fluid Mechanics*, 28(1):11–43, 1996.
- [9] Said Elghobashi. On predicting particle-laden turbulent flows. *Applied scientific research*, 52(4):309–329, 1994.
- [10] Christophe Morel. Mathematical modeling of disperse two-phase flows. 2015.
- [11] Jim Ferry and S Balachandar. Equilibrium expansion for the eulerian velocity of small particles. *Powder Technology*, 125(2-3):131–139, 2002.
- [12] Martin R Maxey and James J Riley. Equation of motion for a small rigid sphere in a nonuniform flow. *The Physics of Fluids*, 26(4):883–889, 1983.

- [13] Joseph Boussinesq. *Théorie analytique de la chaleur mise en harmonie avec la thermodynamique et avec la théorie mécanique de la lumière: Tome I-[II]...*, volume 2. Gauthier-Villars, 1903.
- [14] DN Beaumont. The stability of spatially periodic flows. *Journal of Fluid Mechanics*, 108: 461–474, 1981.
- [15] A Traxler, Stephan Stellmach, Pascale Garaud, T Radko, and N Brummell. Dynamics of fingering convection i: Small-scale fluxes and large-scale instabilities. *arXiv preprint arXiv:1008.1807*, 2010.
- [16] Adrienne Traxler, Pascale Garaud, and Stephan Stellmach. Numerically determined transport laws for fingering (“thermohaline”) convection in astrophysics. *The Astrophysical Journal Letters*, 728(2):L29, 2011.
- [17] Stephan Stellmach, A Traxler, Pascale Garaud, N Brummell, and T Radko. Dynamics of fingering convection ii: The formation of thermohaline staircases. *arXiv preprint arXiv:1008.1808*, 2010.
- [18] Ryan Moll, Pascale Garaud, and Stephan Stellmach. A new model for mixing by double-diffusive convection (semi-convection). iii. thermal and compositional transport through non-layered oddc. *The Astrophysical Journal*, 823(1):33, 2016.
- [19] Pascale Garaud and Logithan Kulenthirarajah. Turbulent transport in a strongly stratified forced shear layer with thermal diffusion. *The Astrophysical Journal*, 821(1):49, 2016.
- [20] Raymond A Shaw. Particle-turbulence interactions in atmospheric clouds. *Annual Review of Fluid Mechanics*, 35(1):183–227, 2003.
- [21] Philip N Segre, Fang Liu, Paul Umbanhowar, and David A Weitz. An effective gravitational temperature for sedimentation. *Nature*, 409(6820):594–597, 2001.
- [22] Pascale Garaud and Sara Nasab. Inertial concentration of dust particles in accretion disks. In *AAS/Division for Extreme Solar Systems Abstracts*, volume 51 of *AAS/Division for Extreme Solar Systems Abstracts*, page 317.09, August 2019.